Electron-spin double resonance of nitrogen-vacancy centers in diamond under a strong driving field

Takumi Mikawa, Ryusei Okaniwa, Yuichiro Matsuzaki, Norio Tokuda, and Junko Ishi-Hayase

Phys. Rev. A **108**, 012610 — Published 10 July 2023

DOI: 10.1103/PhysRevA.108.012610

Electron-spin double resonance of nitrogen-vacancy centers in diamond under a strong driving field

Takumi Mikawa,[1,2,*] Ryusei Okaniwa,[1,2] Yuichiro Matsuzaki,[3,4,†] Norio Tokuda,[5,6] and Junko Ishi-Hayase[1,2,‡]

[1] *School of Fundamental Science and Technology, Keio University, 3-14-1 Hiyoshi, Kohoku-ku, Yokohama, Kanagawa 223-8522 Japan*
[2] *Center for Spintronics Research Network, Keio University, 3-14-1 Hiyoshi, Kohoku-ku, Yokohama, Kanagawa 223-8522 Japan*
[3] *Research Center for Emerging Computing Technologies, National Institute of Advanced Industrial Science and Technology (AIST), 1-1-1 Umezono, Tsukuba, Ibaraki 305-8568, Japan*
[4] *NEC-AIST Quantum Technology Cooperative Research Laboratory, National Institute of Advanced Industrial Science and Technology(AIST), 1-1-1 Umezono, Tsukuba, Ibaraki 305-8568, Japan*
[5] *Graduate School of Natural Science and Technology, Kanazawa University, Kakuma, Kanazawa, Ishikawa 920-1192, Japan*
[6] *Nanomaterials Research Institute, Kanazawa University, Kakuma, Kanazawa, Ishikawa 920-1192, Japan*

(Dated: June 5, 2023)

The nitrogen-vacancy (NV) center in diamond has been the focus of research efforts because of its suitability for use in applications such as quantum sensing and quantum simulations. Recently, the electron-spin double resonance (ESDR) of NV centers has been exploited for detecting radio-frequency (RF) fields with continuous-wave optically detected magnetic resonance. However, the characteristic phenomenon of ESDR under a strong RF field remains to be fully elucidated. In this study, we theoretically and experimentally analyzed the ESDR spectra under strong RF fields by adopting the Floquet theory. Our analytical and numerical calculations could reproduce the ESDR spectra obtained by measuring the spin-dependent photoluminescence under the continuous application of microwaves and an RF field for a DC bias magnetic field perpendicular to the NV axis. We found that anticrossing structures that appear under a strong RF field are induced by the generation of RF-dressed states owing to the two-RF-photon resonances. Moreover, we found that $2n$-RF-photon resonances were allowed by an unintentional DC bias magnetic field parallel to the NV axis. These results should help in the realization of precise MHz-range AC magnetometry with a wide dynamic range beyond the rotating wave approximation regime as well as Floquet engineering in open quantum systems.

I. INTRODUCTION

A nitrogen-vacancy (NV) center in diamond is a point defect composed of a substitutional nitrogen atom adjacent to a vacancy in the carbon lattice [1, 2]. The electronic spin states of an NV center can be initialized by the illumination of a green laser and readout by measuring the spin-dependent photoluminescence. Moreover, the spin state can be manipulated by irradiating microwaves (MW) and exhibits a long coherence time even at room temperature. Owing to these properties, the NV center is a promising system for realizing quantum sensors with high sensitivity and spatial resolution [3–5] as well as feasible quantum simulators [6–8] under ambient conditions.

Quantum sensing and simulation based on NV centers have been demonstrated using optically detected magnetic resonance (ODMR). ODMR has been performed using continuous-wave techniques (CW-ODMR) [9–11] and pulsed techniques [12–15]. In the case of AC magnetic field sensing, several types of pulsed (such as Hahn echo) techniques have been used. However, these techniques suffer from control errors and require careful calibration before measurements [16–18]. In contrast, the CW-ODMR technique is simple and employed widely because it uses continuous laser illumination and MW irradiation and does not require pulse control or careful calibration. However, the detectable frequency of CW-ODMR-based magnetometry is limited to values typically lower than the kHz range.

Recently, we proposed and successfully demonstrated MHz-range AC magnetometry using CW-ODMR [16, 17] by exploiting the phenomenon of electron-spin double resonance (ESDR) of NV centers [16–22]. During the ESDR measurements, we simultaneously and continuously irradiated a radio frequency (RF) field as the target and MW as the probe. If the RF field is coherently coupled to the electron spin states of the NV center, then RF-dressed states are generated, allowing one to probe the states by measuring the CW-ODMR spectrum by sweeping the MW frequencies under an RF field (ESDR spectrum). Thus, ESDR allows for the detection of MHz-range AC magnetic fields without pulse control and high-speed measurements. However, despite these advantages, the characteristic phenomenon of ESDR under a strong RF field remains to be completely elucidated [16–22]. Previous studies of ESDR focused on measuring weak

* Email: mikawa_jukusei@keio.jp
† Email: matsuzaki.yuichiro@aist.go.jp
‡ Email: hayase@appi.keio.ac.jp

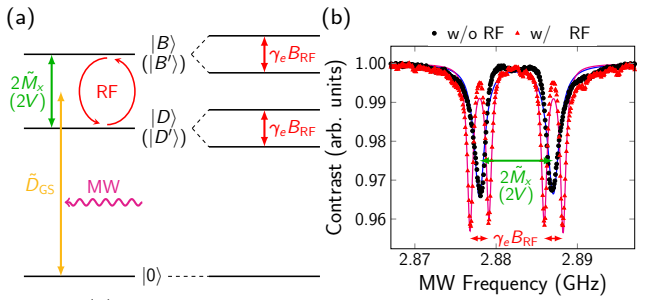

FIG. 1. (a) Energy diagram of electronic spin-triplet ground state of NV center under DC bias magnetic field perpendicular to NV axis under continuous application of MW and RF field. $\tilde{D}_{\rm GS}$ is zero-field splitting, and $\tilde{M}_x$ is effective strain under perpendicular magnetic field. (b) CW-ODMR spectra without and with the radio-frequency (RF) fields for the amplitude $B_{\rm RF} = 69.8\,\mu$T and frequency $\omega_{\rm RF}/(2\pi) = 9.09\,$MHz. In CW-ODMR spectrum under RF field (i.e., ESDR spectrum), four dips are observed owing to creation of RF-dressed states [see (a)]. Solid lines indicate fitting curves calculated using multiple harmonic oscillator model.

RF fields. In the theoretical analysis performed in these studies, the rotating wave approximation (RWA), which is valid only for weak RF fields, played an important role [16–18, 20].

In the present study, we theoretically and experimentally analyzed the ESDR spectra of NV centers under strong RF fields. When driving a system with a strong external field, it is difficult to perform a theoretical analysis because the RWA is violated [23–26]. To solve this problem, we adopted the Floquet theory [27, 28], which can be used to treat quantum systems driven by the time-periodic Hamiltonian [29–31]. The Floquet theory provides more precise solutions beyond the RWA regime, can account for muti-photon transitions, and yields further insights [32–37]. Using the Floquet theory, we calculated the ESDR spectra under both weak and strong RF fields. Moreover, we performed ESDR experiments and found that the numerical and experimental results were in good agreement. Thus, our results should aid the realization of more precise MHz-range AC magnetometry with a wider dynamic range using CW-OMDR, fast and precise quantum control beyond the RWA regime [24, 25, 36, 37], and simulations of various quantum phenomena under strong driving fields [6, 38, 39]. In particular, the NV center can be treated as a single-body system resistant to dissipation and is expected to serve as a platform for the Floquet engineering in open quantum systems [40–42].

II. THEORY

A. Single RF-photon resonances

In this section, we review the previous work about ESDR under a weak RF field in Ref. [16, 17]. We applied a DC bias magnetic field perpendicular to the NV axis. It should be noted that the bias magnetic field contributes to suppressing inhomogeneous broadening owing to random magnetic fields [43]. For $M_x \ll \gamma_e B_x, \gamma_e B_y \ll D_{\rm GS}$, the electronic spin-triplet (S = 1) ground state Hamiltonian of the NV center without an external oscillating field can be written as ($\hbar = 1$) follows: [17, 18]

$$\hat{H}_0 \approx \tilde{D}_{\rm GS}\hat{S}_z^2 + \tilde{M}_x(\hat{S}_x^2 - \hat{S}_y^2), \tag{1}$$

where $\hat{\boldsymbol{S}} = (\hat{S}_x, \hat{S}_y, \hat{S}_z)$ is the dimensionless spin-1 operators for the electronic spin. Here, we consider the direction of the effective strain to be the x direction. Furthermore, $\tilde{D}_{\rm GS}$ is the zero-field splitting, and $\tilde{M}_x$ is the effective strain under the perpendicular magnetic field [17] (Appendix A for details). Under the perpendicular DC bias field, the eigenstates can be approximated as $|B\rangle := (|m_s = +1\rangle + |m_s = -1\rangle)/\sqrt{2}$ and $|D\rangle := (|m_s = +1\rangle - |m_s = -1\rangle)/\sqrt{2}$ and $|m_s = 0\rangle$ [16, 17, 44]. The energy diagram is shown in Fig. 1(a).

For the ESDR, we assumed simultaneous irradiation with MW and an RF field. In this case, the Hamiltonian is given by

$$\begin{aligned}\hat{H}(t) \approx{}& \tilde{D}_{\rm GS}\hat{S}_z^2 + \tilde{M}_x(\hat{S}_x^2 - \hat{S}_y^2) \\ &+ (2\lambda^b\hat{S}_x + 2\lambda^d\hat{S}_y)\cos\omega_{\rm MW}t \\ &+ 2\Omega_{\rm RF}\hat{S}_z\cos\omega_{\rm RF}t,\end{aligned} \tag{2}$$

where λ^b (λ^d) is the amplitude of the MW in the x (y) direction, $\Omega_{\rm RF}$ is the amplitude of the RF field in the z direction, and $\omega_{\rm MW}$ ($\omega_{\rm RF}$) is the MW (RF) frequency. Here, we ignore the longitudinal components of the MW and the transverse components of the RF field because they oscillate with a high frequency without any resonance. In addition, we move to a rotating frame defined by $\hat{R}_0(t) = e^{-i\omega_{\rm MW}\hat{S}_z^2}$. By using the RWA, we can rewrite this Hamiltonian as

$$\begin{aligned}\hat{H}(t) \approx{}& \Delta_{\rm MW}\hat{S}_z^2 + \tilde{M}_x(\hat{S}_x^2 - \hat{S}_y^2) \\ &+ \lambda^b\hat{S}_x + \lambda^d\hat{S}_y + 2\Omega_{\rm RF}\hat{S}_z\cos\omega_{\rm RF}t,\end{aligned} \tag{3}$$

where $\Delta_{\rm MW} := \tilde{D}_{\rm GS} - \omega_{\rm MW}$ is detuning. To derive Eq. (3), we drop the high-oscillation term, that is, $e^{\pm 2i\omega_{\rm MW}t}$. Because $2\omega_{\rm MW}$ is significantly larger than any of the parameters in Eq. (3) except the zero-field splitting, $\tilde{D}_{\rm GS}$, we assumed that this approximation would be valid throughout this study.

The Hamiltonian in Eq. (3) is periodic in time. Thus, we can adopt the Floquet theory to describe the dynamics beyond the RWA regime. By using the Floquet theory, we obtain a time-independent Hamiltonian instead of a time-periodic one (See Appendix B for details). To simplify the notation, we use the extended Hilbert space or the Sambe space, $\mathfrak{F}$ [28]. Then, we can express the time-independent Hamiltonian using the basis of $|\alpha, n\rangle = |\alpha\rangle\otimes|n\rangle$, where α is the state of the NV center, and n is the Fourier index. In this case, the Fourier index, n can be interpreted as the number of absorbed RF

photons (if n is negative, $|n| = -n$ can be interpreted as the number of emitted RF photons) [29]. Thus, we can treat $|n\rangle$ as the Fock state. In the Sambe space, the quantum dynamics can be described using the Floquet Hamiltonian $\hat{H}_F$ as follows

$$\hat{H}_F := \sum_m \hat{\mathcal{F}}_m \otimes \hat{H}^{(m)} + \hat{\mathcal{N}} \otimes \omega_{\mathrm{RF}} \hat{1}, \tag{4}$$

where $\hat{\mathcal{F}}_n$ are the Floquet ladder operators, $\hat{\mathcal{N}}$ is the Floquet number operator, and $\hat{H}^{(m)}$ is the Fourier coefficient. These are defined as follows [31]:

$$\hat{\mathcal{F}}_n |m\rangle = |n+m\rangle, \tag{5}$$

$$\hat{\mathcal{N}} |n\rangle = n |n\rangle, \tag{6}$$

$$\hat{H}(t) = \sum_m \hat{H}^{(m)} e^{im\omega_{\mathrm{RF}} t}. \tag{7}$$

For the ESDR, the Floquet Hamiltonian can be represented by the matrix using the basis of $\{|B\rangle, |0\rangle, |D\rangle\}$ as follows:

$$\hat{H}_F = \left[\begin{array}{ccc|ccc|ccc|c}
\ddots & \vdots & \vdots & \vdots & \vdots & \vdots & & & & \\
\cdots & \Delta^b_{\mathrm{MW}} + \omega_{\mathrm{RF}} & \lambda^b & 0 & 0 & 0 & \Omega_{\mathrm{RF}} & & & \\
\cdots & \lambda^b & \omega_{\mathrm{RF}} & i\lambda^d & 0 & 0 & 0 & & & \\
\cdots & 0 & -i\lambda^d & \Delta^d_{\mathrm{MW}} + \omega_{\mathrm{RF}} & \Omega_{\mathrm{RF}} & 0 & 0 & & & \\
\hline
\cdots & 0 & 0 & \Omega_{\mathrm{RF}} & \Delta^b_{\mathrm{MW}} & \lambda^b & 0 & 0 & 0 & \Omega_{\mathrm{RF}} & \cdots \\
\cdots & 0 & 0 & 0 & \lambda^b & 0 & i\lambda^d & 0 & 0 & 0 & \cdots \\
\cdots & \Omega_{\mathrm{RF}} & 0 & 0 & 0 & -i\lambda^d & \Delta^d_{\mathrm{MW}} & \Omega_{\mathrm{RF}} & 0 & 0 & \cdots \\
\hline
 & & & & 0 & 0 & \Omega_{\mathrm{RF}} & \Delta^b_{\mathrm{MW}} - \omega_{\mathrm{RF}} & \lambda^b & 0 & \cdots \\
 & & & & 0 & 0 & 0 & \lambda^b & -\omega_{\mathrm{RF}} & i\lambda^d & \cdots \\
 & & & & \Omega_{\mathrm{RF}} & 0 & 0 & 0 & -i\lambda^d & \Delta^d_{\mathrm{MW}} - \omega_{\mathrm{RF}} & \cdots \\
\hline
 & & & & \vdots & \vdots & \vdots & \vdots & \vdots & \vdots & \ddots
\end{array}\right]
\begin{array}{l}
\vdots \\
\leftarrow |B,+1\rangle \\
\leftarrow |0,+1\rangle \\
\leftarrow |D,+1\rangle \\
\leftarrow |B,0\rangle \\
\leftarrow |0,0\rangle \\
\leftarrow |D,0\rangle \\
\leftarrow |B,-1\rangle \\
\leftarrow |0,-1\rangle \\
\leftarrow |D,-1\rangle \\
\vdots
\end{array} \tag{8}$$

where $\Delta^b_{\mathrm{MW}} := \Delta_{\mathrm{MW}} + \tilde{M}_x, \Delta^d_{\mathrm{MW}} := \Delta_{\mathrm{MW}} - \tilde{M}_x$.

The time-averaged transition probability from $|\alpha\rangle$ to $|\beta\rangle$ is calculated as follows:

$$\langle P_{\alpha\to\beta} \rangle = \sum_{n,m} \sum_k |\langle \beta, n | q_k, m \rangle|^2 |\langle q_k, m | \alpha, 0 \rangle|^2, \tag{9}$$

where $|q_k, m\rangle$ are the eigenstates of the Floquet Hamiltonian [27]. To obtain $|q_k, m\rangle$, we must solve the infinite-dimensional eigenvalue equation (See Eqs. (B6) and (B4) for the details). Specifically, by truncating the Floquet Hamiltonian to a finite size, we can calculate the transition probability through a numerical simulation.

When the ESDR condition $|\omega_{\mathrm{RF}} - 2\tilde{M}_x| \ll \Omega_{\mathrm{RF}}$ is satisfied, $|B, n\rangle$ and $|D, n+1\rangle$ can be coupled to the RF field, and a single-RF-photon resonance occurs. Focusing on the single-RF-photon resonance (e.g., that between $|B, 0\rangle$ and $|D, +1\rangle$) we can reduce the infinite-dimensional Floquet Hamiltonian in Eq. (8) a 3×3 effective Hamiltonian:

$$\hat{H}_{\mathrm{eff}} \approx \begin{bmatrix} \Delta^b_{\mathrm{MW}} & \lambda^b & \Omega_{\mathrm{RF}} \\ \lambda^b & 0 & 0 \\ \Omega_{\mathrm{RF}} & 0 & \Delta^d_{\mathrm{MW}} + \omega_{\mathrm{RF}} \end{bmatrix}. \tag{10}$$

This matrix can also be derived from Eq. (3) without the Floquet theory by using the RWA in the rotating frame defined by $e^{-i\omega_{\mathrm{RF}} t |D\rangle\langle D|}$, as in Ref. [17]. Using Fermi's golden rule or the harmonic oscillator model [17, 18, 44] under the weak driving condition $\Omega_{\mathrm{RF}} \ll \omega_{\mathrm{RF}}$, we can obtain the resonant MW frequencies [16, 17], as follows:

$$\omega_{\mathrm{MW}} = \tilde{D}_{\mathrm{GS}} + \frac{1}{2}\omega_{\mathrm{RF}} \pm \sqrt{\left(\tilde{M}_x - \frac{1}{2}\omega_{\mathrm{RF}}\right)^2 + \Omega^2_{\mathrm{RF}}}. \tag{11}$$

Similarly, focusing on $|B, -1\rangle$ and $|D, 0\rangle$, we obtain another analytical solution, as follows:

$$\omega_{\mathrm{MW}} = \tilde{D}_{\mathrm{GS}} - \frac{1}{2}\omega_{\mathrm{RF}} \pm \sqrt{\left(\tilde{M}_x - \frac{1}{2}\omega_{\mathrm{RF}}\right)^2 + \Omega^2_{\mathrm{RF}}}, \tag{12}$$

which can also be derived from Eq. (3) by the RWA in the rotating frame defined using $e^{i\omega_{\mathrm{RF}} t |B\rangle\langle B|}$. Equations (11) and (12) indicate that the anticrossings occur at the RF frequency $\omega_{\mathrm{RF}} \approx 2\tilde{M}_x$. These anticrossing gaps are called the Aulter–Towns splittings [17, 20, 45] and are proportional to the RF amplitude Ω_{RF}. Thus, upon the irradiation of a resonant RF field, we observed four dips in the

CW-ODMR spectrum (i.e., ESDR spectrum) with the Aulter–Towns splittings $2\Omega_{\rm RF} = \gamma_e B_{\rm RF}$ (See Fig. 1(b)), which allowed for MHz-range AC magnetic field sensing [16, 17].

B. Multi-RF-photon resonances

Next, we consider ESDR under a strong RF field $\Omega_{\rm RF} \gtrsim \omega_{\rm RF}$, which results in multi-RF-photon resonances. The simple model for using the RWA [16, 17] does not explain these phenomena, while the Floquet theory can reproduce the experimental results in this regime, as described later. In the case of a single-RF-photon resonance, the non-zero off-diagonal terms with $\Omega_{\rm RF} \neq 0$ in the Floquet Hamiltonian induce the transition between $|B, n\rangle$ and $|D, n+1\rangle$. Here, the RF photon number, n, changes with $\Delta m = +1$. On the other hand, other transitions also occur between the states with different RF photon numbers in the case of multi-RF-photon resonances. The key point is that even when the off-diagonal terms between the states in the Floquet Hamiltonian are zero, the transitions between the specific states can occur via indirect transitions that use the other states as the intermediate states.

Let us consider an example of one such indirect transition owing to strong RF driving. In Eq. (8), there is an indirect transition between $|B, -1\rangle$ and $|B, +1\rangle$. Let us focus on this transition. While there are no direct transitions between $|B, -1\rangle$ and $|B, +1\rangle$, we can induce a transition from $|B, -1\rangle$ to $|D, 0\rangle$ and subsequently induce a transition from $|D, 0\rangle$ to $|B, +1\rangle$. In this case, the quantum number, n, changes by $+2$, which corresponds to the two-RF-photon transitions. It should be noted that, during the transition described above, the spin state does not change, thus the so-called anticrossing is not observed during the spectroscopy. In addition, more RF-photon transitions can occur if we consider higher-order transitions, including three-RF-photon transitions through a sequence of transitions, such as $|B, -2\rangle \to |D, -1\rangle \to |B, 0\rangle \to |D, +1\rangle$. In this case, an anticrossing structure should be observed since the spin state is changed. By performing similar calculations, we can show that $2n$-RF-photon transitions from $|B, -1\rangle$ to $|B, 2n-1\rangle$ cannot induce the anticrossing structures while $(2n-1)$-RF-photon transitions from $|B, -2\rangle$ to $|D, 2n-1\rangle$ can.

Importantly, if we consider the effect of the DC bias magnetic field parallel to the NV axis, $\omega_L := \gamma_e B_z^{(\rm bias)}$, additional anticrossing structures occur owing to the multi-RF-photon resonances. Such magnetic fields may originate because of the misalignment of the perpendicular bias magnetic field or the Earth's magnetic field ($\approx 0.05\,\mathrm{mT}$). The Hamiltonian under the bias magnetic field in the absence of drivings is given as

$$\hat{H}_0' = \tilde{D}_{\rm GS}\hat{S}_z^2 + \tilde{M}_x(\hat{S}_x^2 - \hat{S}_y^2) + \omega_L \hat{S}_z. \tag{13}$$

The lowest-energy eigenstate of this Hamiltonian is $|0\rangle$ with an eigenenergy of 0. The other eigenstates of this Hamiltonian are as follows:

$$\begin{aligned} |B'\rangle &:= \frac{(\tilde{M}_x + V)\,|B\rangle + \omega_L\,|D\rangle}{\sqrt{(\tilde{M}_x + V)^2 + \omega_L^2}}, \\ |D'\rangle &:= \frac{-\omega_L\,|B\rangle + (\tilde{M}_x + V)\,|D\rangle}{\sqrt{(\tilde{M}_x + V)^2 + \omega_L^2}}, \end{aligned} \tag{14}$$

with eigenvalues of $\tilde{D}_{\rm GS} + V$ and $\tilde{D}_{\rm GS} - V$, respectively where $V := \sqrt{\tilde{M}_x^2 + \omega_L^2}$. By using this basis, the Hamiltonian of the NV center including the MW and the RF field is expressed as

$$\begin{aligned} \hat{H}(t) \approx{}& \tilde{D}_{\rm GS}\hat{S}_z^2 + \tilde{M}_x(\hat{S}_x^2 - \hat{S}_y^2) + \omega_L \hat{S}_z \\ &+ (2\lambda^b \hat{S}_x + 2\lambda^d \hat{S}_y)\cos\omega_{\rm MW} t \\ &+ 2\Omega_{\rm RF}\hat{S}_z \cos\omega_{\rm RF} t. \end{aligned} \tag{15}$$

In the rotating frame defined by $\hat{R}_0(t)$, we adopt the RWA for the MW; then the Hamiltonian is represented as

$$\hat{H}'(t) \approx \begin{bmatrix} \Delta_{\rm MW} + V + 2\dfrac{\omega_L \Omega_{\rm RF}}{V}\cos\omega_{\rm RF} t & \lambda^{b'} & 2\dfrac{\tilde{M}_x \Omega_{\rm RF}}{V}\cos\omega_{\rm RF} t \\ (\lambda^{b'})^* & 0 & i\lambda^{d'} \\ 2\dfrac{\tilde{M}_x \Omega_{\rm RF}}{V}\cos\omega_{\rm RF} t & -i(\lambda^{d'})^* & \Delta_{\rm MW} - V - 2\dfrac{\omega_L \Omega_{\rm RF}}{V}\cos\omega_{\rm RF} t \end{bmatrix}, \tag{16}$$

where $\lambda^{b'} := \dfrac{(\tilde{M}_x + V)\lambda^b - i\omega_L \lambda^d}{\sqrt{(\tilde{M}_x + V)^2 + \omega_L^2}}$ $\left[\lambda^{d'} := \dfrac{i\omega_L \lambda^b + (\tilde{M}_x + V)\lambda^d}{\sqrt{(\tilde{M}_x + V)^2 + \omega_L^2}}\right]$ is the effective MW amplitude corresponding to the transition between $|0\rangle$ and $|B'\rangle$ ($|D'\rangle$). Similar to the derivation of Eq. (3), for the RWA to be valid, the effective MW amplitude should be much smaller than the MW frequency, that is, $|\lambda^b|, |\lambda^d| \ll \omega_{\rm MW}$. We assume that this condition is always satisfied throughout this paper. From the Fourier expansion, the Floquet Hamiltonian for the

ESDR can be represented as follows:

$$\hat{H}'_F = \left[\begin{array}{ccccccccccc}
\ddots & \vdots & \vdots & \vdots & \vdots & \vdots & \vdots & & & & \\
\hline
\cdots & \Delta_1^{b'} & \lambda^{b'} & 0 & \omega_L\Omega_{\mathrm{RF}}/V & 0 & \tilde{M}_x\Omega_{\mathrm{RF}}/V & & & & \\
\cdots & (\lambda^{b'})^* & \omega_{\mathrm{RF}} & i\lambda^{d'} & 0 & 0 & 0 & & & & \\
\cdots & 0 & (i\lambda^{d'})^* & \Delta_1^{d'} & \tilde{M}_x\Omega_{\mathrm{RF}}/V & 0 & -\omega_L\Omega_{\mathrm{RF}}/V & & & & \\
\hline
\cdots & \omega_L\Omega_{\mathrm{RF}}/V & 0 & \tilde{M}_x\Omega_{\mathrm{RF}}/V & \Delta_0^{b'} & \lambda^{b'} & 0 & \omega_L\Omega_{\mathrm{RF}}/V & 0 & \tilde{M}_x\Omega_{\mathrm{RF}}/V & \cdots \\
\cdots & 0 & 0 & 0 & (\lambda^{b'})^* & 0 & i\lambda^{d'} & 0 & 0 & 0 & \cdots \\
\cdots & \tilde{M}_x\Omega_{\mathrm{RF}}/V & 0 & -\omega_L\Omega_{\mathrm{RF}}/V & 0 & (i\lambda^{d'})^* & \Delta_0^{d'} & \tilde{M}_x\Omega_{\mathrm{RF}}/V & 0 & -\omega_L\Omega_{\mathrm{RF}}/V & \cdots \\
\hline
 & & & & \omega_L\Omega_{\mathrm{RF}}/V & 0 & \tilde{M}_x\Omega_{\mathrm{RF}}/V & \Delta_{-1}^{b'} & \lambda^{b'} & 0 & \cdots \\
 & & & & 0 & 0 & 0 & (\lambda^{b'})^* & -\omega_{\mathrm{RF}} & i\lambda^{d'} & \cdots \\
 & & & & \tilde{M}_x\Omega_{\mathrm{RF}}/V & 0 & -\omega_L\Omega_{\mathrm{RF}}/V & 0 & (i\lambda^{d'})^* & \Delta_{-1}^{d'} & \cdots \\
\hline
 & & & & \vdots & \vdots & \vdots & \vdots & \vdots & \vdots & \ddots
\end{array}\right], \tag{17}$$

where $\Delta_n^{b'} \coloneqq \Delta_{\mathrm{MW}} + V + n\omega_{\mathrm{RF}}$ and $\Delta_n^{d'} \coloneqq \Delta_{\mathrm{MW}} - V + n\omega_{\mathrm{RF}}$.

Then, the new off-diagonal terms, $\omega_L\Omega_{\mathrm{RF}}/V$ allow other subsequent transitions, such as $|B,-1\rangle \to |B,0\rangle \to |D,+1\rangle$. These subsequent transitions indicate that the anticrossing structures owing to the two-RF-photon resonances are created approximately at half the RF frequency at which the single-RF-photon resonances occur.

C. Analytical solutions

To obtain an approximate analytical solution for the resonant frequency of these two-RF-photon resonances, we use the Jacobi-Anger expansion [46, 47]. This method allows for the conversion of multistep single-photon transitions into direct multi-photon transitions. Before calculating the Floquet Hamiltonian of the ESDR, we move to a rotating frame with a siary operator defined as

$$\hat{U} = \exp\left[i\frac{2\omega_L\Omega_{\mathrm{RF}}}{\omega_{\mathrm{RF}}V}\sin\omega_{\mathrm{RF}}t(|B'\rangle\langle B'| - |D'\rangle\langle D'|)\right]. \tag{18}$$

Then, the Hamiltonian in Eq.(16) becomes

$$\hat{H}_I(t) = \begin{bmatrix} \Delta_{\mathrm{MW}}^{b'} & \sum_k \lambda_k^{b'} e^{ik\omega_{\mathrm{RF}}t} & \sum_k \Omega_k e^{ik\omega_{\mathrm{RF}}t} \\ \sum_k (\lambda_k^{b'})^* e^{-ik\omega_{\mathrm{RF}}t} & 0 & i\sum_k \lambda_k^{d'} e^{ik\omega_{\mathrm{RF}}t} \\ \sum_k \Omega_k e^{-ik\omega_{\mathrm{RF}}t} & -i\sum_k (\lambda_k^{d'})^* e^{-ik\omega_{\mathrm{RF}}t} & \Delta_{\mathrm{MW}}^{d'} \end{bmatrix}, \tag{19}$$

where $\lambda_k^{b'} \coloneqq \lambda^{b'} J_k\left(\frac{2\omega_L\Omega_{\mathrm{RF}}}{\omega_{\mathrm{RF}}V}\right), \lambda_k^{d'} \coloneqq \lambda^{d'} J_k\left(\frac{2\omega_L\Omega_{\mathrm{RF}}}{\omega_{\mathrm{RF}}V}\right), \Omega_k \coloneqq \frac{k\omega_{\mathrm{RF}}\tilde{M}_x}{2\omega_L} J_k\left(\frac{4\omega_L\Omega_{\mathrm{RF}}}{\omega_{\mathrm{RF}}V}\right)$.

We used

$$\begin{aligned} e^{i\frac{x}{\omega}\sin\omega t} &= \sum_{k=-\infty}^{\infty} J_k(x)e^{ik\omega t}, \\ J_{k-1}(x) + J_{k+1}(x) &= \frac{2k}{x}J_k(x), \end{aligned} \tag{20}$$

where $J_k(x)$ is the k-th order Bessel function of the first kind. For the RF-dressed states generated by the coupling between $|B,m\rangle$ and $|D,n\rangle$, we move to the rotating frame defined by $e^{-i\omega_{\mathrm{RF}}t(m|B'\rangle\langle B'| + n|D'\rangle\langle D'|)}$ and we use the RWA, wherein we ignore all the oscillating terms [32, 33, 48]. Then, we obtain the time-independent Hamiltonian as follows:

$$\hat{H}_{\mathrm{RWA}} \approx \begin{bmatrix} \Delta_m^{b'} & \lambda_m^{b'} & \Omega_{m-n} \\ (\lambda_m^{b'})^* & 0 & i\lambda_{-n}^{d'} \\ \Omega_{m-n} & (i\lambda_{-n}^{d'})^* & \Delta_n^{d'} \end{bmatrix}. \tag{21}$$

Since the MW driving is weak, we assume that $\lambda_k^{b'} \simeq 0$ and $\lambda_k^{d'} \simeq 0$. In this case, we can analytically diagonalize the Hamiltonian in Eq. (21). Based on the energy difference between the ground and excited state, we obtain the resonant frequency as follows:

$$\omega_{\mathrm{MW}} \approx \tilde{D}_{\mathrm{GS}} + \frac{m+n}{2}\omega_{\mathrm{RF}} \pm \sqrt{\left(V + \frac{m-n}{2}\omega_{\mathrm{RF}}\right)^2 + \Omega_{m-n}^2}. \tag{22}$$

When the resonant condition $\Delta_m^{b'} \approx \Delta_n^{d'}$ is satisfied, the $(m-n)$-RF-photon resonance occurs and generates the RF-dressed states, which exhibit an energy split of $2\Omega_{m-n}$. The RWA is valid when $\lambda_k^{b'}$ and $\lambda_k^{d'}$ are much smaller than ω_{RF}. In addition, as we increase Ω_{RF}, the Bessel functions, $J_k\left(\frac{2\omega_L\Omega_{\mathrm{RF}}}{\omega_{\mathrm{RF}}V}\right)$ and $J_k\left(\frac{4\omega_L\Omega_{\mathrm{RF}}}{\omega_{\mathrm{RF}}V}\right)$, become smaller, and the RWA becomes more accurate [48]. However, since it is experimentally difficult to realize such an ultra-strong RF driving regime, confirming this was out of the scope of this study.

RWA is valid when the off-diagonal component Ω_{m-n} is much smaller than the oscillating frequency, ω_{RF}. Therefore, as we increase the amplitude of the RF driving, the approximation breaks down. As a result, we cannot explain some of the resonances by using this analytical solution. On the other hand, the numerical results with the Floquet theory are still valid even for strong RF driving.

To overcome the limitations of the RWA, we use the van Vleck (vV) transformation [31, 49, 50]. When calculating the effective Hamiltonian Eq. (21) up to the second-order correction using the vV transformation, we obtain

$$\hat{H}_{\mathrm{vV}} \approx \hat{H}_{\mathrm{vV}}^{(1)} + \hat{H}_{\mathrm{vV}}^{(2)} = \begin{bmatrix} \Delta_m^{b'} + \delta_{m,n}^{b'} & \lambda_m^{b'} & \Omega_{m-n} \\ (\lambda_m^{b'})^* & \delta_{m,n}^0 & i\lambda_{-n}^{d'} \\ \Omega_{m-n} & -i(\lambda_{-n}^{d'})^* & \Delta_n^{d'} + \delta_{m,n}^{d'} \end{bmatrix}, \tag{23}$$

where

$$\delta_{m,n}^{b'} \coloneqq \sum_{k\neq 0} \frac{\Omega_{k-m+n}^2 - \Omega_{k+m-n}^2 + |\lambda_{k-m}^{b'}|^2 - |\lambda_{k+m}^{b'}|^2}{2k\omega_{\mathrm{RF}}} \tag{24}$$

$$\delta_{m,n}^{0} \coloneqq \sum_{k\neq 0} \frac{|\lambda_{k+m}^{b'}|^2 - |\lambda_{k-m}^{b'}|^2 - |\lambda_{k+n}^{d'}|^2 + |\lambda_{k-n}^{d'}|^2}{2k\omega_{\mathrm{RF}}} \tag{25}$$

$$\delta_{m,n}^{d'} \coloneqq \sum_{k\neq 0} \frac{\Omega_{k+m-n}^2 - \Omega_{k-m+n}^2 + |\lambda_{k-n}^{d'}|^2 - |\lambda_{k+n}^{d'}|^2}{2k\omega_{\mathrm{RF}}}. \tag{26}$$

By calculating the energy difference between the ground and excited states, we obtain the resonant MW frequencies as

$$\omega_{\mathrm{MW}} \approx \tilde{D}_{\mathrm{GS}} - \delta_{m,n}^0 + \frac{m+n}{2}\omega_{\mathrm{RF}} \pm \sqrt{\left(V + \frac{\delta_{m,n}^{b'} - \delta_{m,n}^{d'}}{2} + \frac{m-n}{2}\omega_{\mathrm{RF}}\right)^2 + \Omega_{m-n}^2}. \tag{27}$$

By including the higher-order corrections described in Eq. (17), we can obtain a more accurate analytical solution. This is left for a future work study.

III. RESULT

A. Setup

To verify this theory, we performed experiments using a home-built confocal laser microscope setup with NV ensembles, as in Ref. [18]. The diamond sample used was a N-doped CVD-grown NV layer with a thickness of 4.9 µm on a (111)-oriented diamond substrate. The NV concentration was estimated to be $\sim 10^{16}\,\mathrm{cm}^{-3}$. The NV orientation was preferentially aligned along the [111] direction of the diamond lattice [51–54]. The NV ensembles were excited using a 532 nm green laser with an average power of 0.080 mW. The spin-dependent photoluminescence was measured using an avalanche photodiode under the continuous application of MW and RF fields to obtain the CW-ODMR spectra under ESDR conditions (i.e., the ESDR spectra). The MW was irradiated at a power of −30 dB from an MW antenna placed on the opposite side of the NV layer [55]. The RF field was irradiated by placing a copper wire on the NV layer. During all the ESDR experiments performed in this study, we swept the MW frequency for different RF frequencies and amplitudes under a DC bias magnetic field perpendicular to the NV axis.

B. Preliminary experiment without RF field

As a preliminary experiment, we measured the CW-ODMR spectrum without an RF field. As shown in Fig. 1(b), we observed two dips corresponding to the two resonances. One of them corresponds to a transition from $|0\rangle$ to $|B'\rangle$, while the other corresponds to a transition from $|0\rangle$ to $|D'\rangle$. This ODMR spectrum could be fitted using a harmonic oscillator model [17, 18, 44]. From the fitting, we obtained $\tilde{D}_{\mathrm{GS}}/(2\pi) = 2.8825$ GHz (zero-field splitting), $2V = 9.09$ MHz (the resonant frequency between $|B'\rangle$ and $|D'\rangle$), and $\lambda^b/(2\pi) = \lambda^d/(2\pi) = 0.12$ MHz (the MW amplitudes).

C. Weak RF regime

Next, we performed the ESDR experiment under a weak RF field with $\Omega_{\mathrm{RF}}/(2\pi) \approx 1.96$ MHz ($B_{\mathrm{RF}} =$

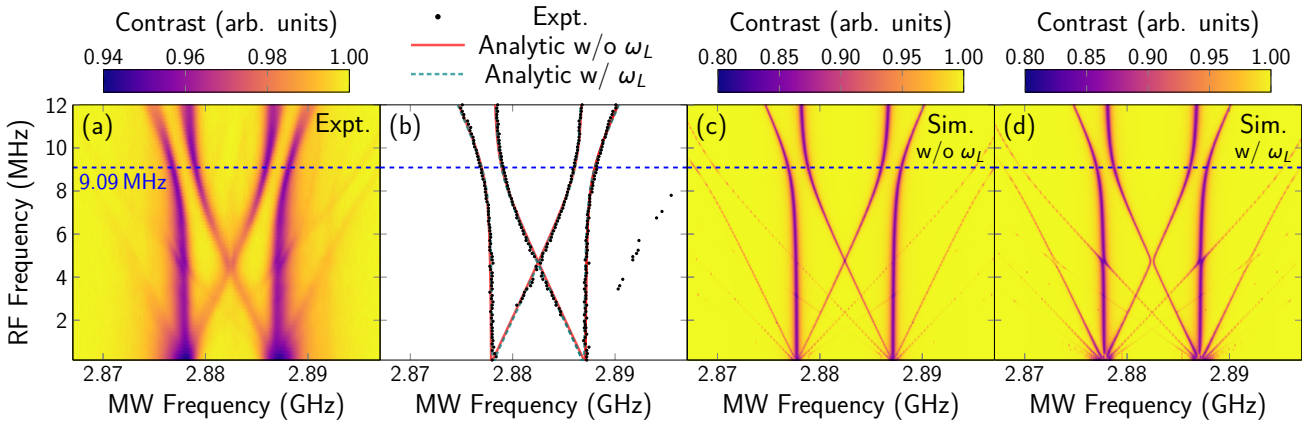

FIG. 2. (a) ESDR spectra under DC bias magnetic field perpendicular to NV axis as measured by sweeping MW and RF frequencies for a weak RF field with $B_{\mathrm{RF}} = 69.8\,\mu\mathrm{T}$. (b) Comparison of the resonant frequencies obtained experimentally and those obtained from analytical solutions under a weak RF field. Experimental resonant frequencies were extracted from (a), while analytical solutions without and with parallel DC bias magnetic field ω_L were obtained using Eqs. (11),(12), and (22). (c) and (d) Results of numerical simulations performed using Floquet Hamiltonian (c) without and (d) with parallel DC bias magnetic field. Parameters used for simulation in (c) [(d)] are $\tilde{D}_{\mathrm{GS}}/(2\pi) = 2.8825\,\mathrm{GHz}$, $\tilde{M}_x/(2\pi) = 9.09\,\mathrm{MHz}/2$ [$\tilde{M}_x/(2\pi) = 4.40\,\mathrm{MHz}$, $\omega_L/(2\pi) = 0.50\,\mathrm{MHz}$] and $\lambda^{b'}/(2\pi) = \lambda^{a'}/(2\pi) = 0.12\,\mathrm{MHz}$. Dashed lines in (a) and (b) indicate resonant frequency between $|B\rangle$ ($|B'\rangle$) and $|D\rangle$ ($|D'\rangle$), anticrossing structures emerge near dashed lines. There is good agreement between experimental and analytical results, and parallel bias magnetic field had no effect under the weak RF field.

69.8 µT), which satisfied the RWA condition for single-RF-photon resonances, $\Omega_{\mathrm{RF}} \ll 2\tilde{M}_x(2V)$. Under the continuous application of MW and the RF field, we measured the ESDR spectra while setting the amplitude of the RF field at $B_{\mathrm{RF}} = 69.8\,\mu\mathrm{T}$ and varying its frequency. The results are shown in Fig 2(a). anticrossing structures were observed when we set $\omega_{\mathrm{RF}}/(2\pi) = 9.09\,\mathrm{MHz}$ [dashed line in Fig. 2(a)]. The corresponding ESDR spectra are shown in Fig. 2(b). This result indicates the formation of RF-dressed states. Importantly, we did not observe a clear anticrossing behavior near the RF frequency of $\omega_{\mathrm{RF}}/(2\pi) = 4.5\,\mathrm{MHz}$ under the weak RF field. Here, we considered the effect of a parallel DC magnetic field in the calculations, because an unintentional parallel DC magnetic field may have been applied in the actual experiment.

Using Eq. (9), we numerically simulate the ESDR spectra without (with) a parallel DC bias magnetic field, ω_L, as shown in Fig 2(c) [Fig. 2(d)]. We then truncated the Floquet Hamiltonians in Eqs. (8) and (17) to 405×405 matrixes and set $\tilde{M}_x/(2\pi) = 4.40\,\mathrm{MHz}$ and $\omega_L/(2\pi) = 0.60\,\mathrm{MHz}$. Here, the parallel DC magnetic field, $B_z^{(\mathrm{bias})} = \omega_L/\gamma_e \approx 0.02\,\mathrm{mT}$, is relatively small compared with the Earth's magnetic field of $\approx 0.05\,\mathrm{mT}$. This is because the effect of the Earth's magnetic field and the misalignment of the perpendicular DC magnetic field probably cancel each other. Moreover, we extracted the resonant MW frequencies from Fig. 2(a) and compared them with the analytical solutions obtained using Eqs. (11), (12), and (22), as shown in Fig. 2(b).

With respect to the resonant MW frequencies, both the numerical and analytical solutions agreed with the experimental result. However, there was a small deviation between the experimental and theoretical results in the case of the contrast and linewidth. This is because we did not consider the effect of the initialization by the laser and the decoherence for simplicity. More importantly, we did not observe any significant differences between the numerical simulations performed with and without the parallel bias magnetic field, ω_L, with respect to the resonant frequencies in the weak RF regime, $\Omega_{\mathrm{RF}} \ll 2\tilde{M}_x(2V)$. This is because the parallel magnetic field induces multi-RF-photon resonances but does not significantly affect single-RF-photon resonances. We observed the anticrossing structures under the parallel bias magnetic field. However, the splitting of the anticrossing structures under the weak RF field was much smaller than that under the strong RF field, as discussed in Sec. III D.

D. Strong RF regime

In the second experiment, we applied a strong RF field with an amplitude of $B_{\mathrm{RF}} = 136.8\,\mu\mathrm{T}$ and measured the ESDR spectra while varying the frequency of the RF field. The RWA condition began to collapse owing to the large RF amplitude, Ω_{RF}. Figure 3(a) shows the experimental results under the strong RF field. Similar to the case for the ESDR spectra under the weak RF field, the anticrossing structures corresponding to the single-RF-photon resonances were observed around the RF frequency, $\omega_{\mathrm{RF}}/(2\pi) = 9.09\,\mathrm{MHz}$, with large splitting energy as indicated by the dashed line in Fig. 3(a). In contrast to the weak RF regime, we observed additional anticrossing structures when the RF frequency, $\omega_{\mathrm{RF}}/(2\pi)$,

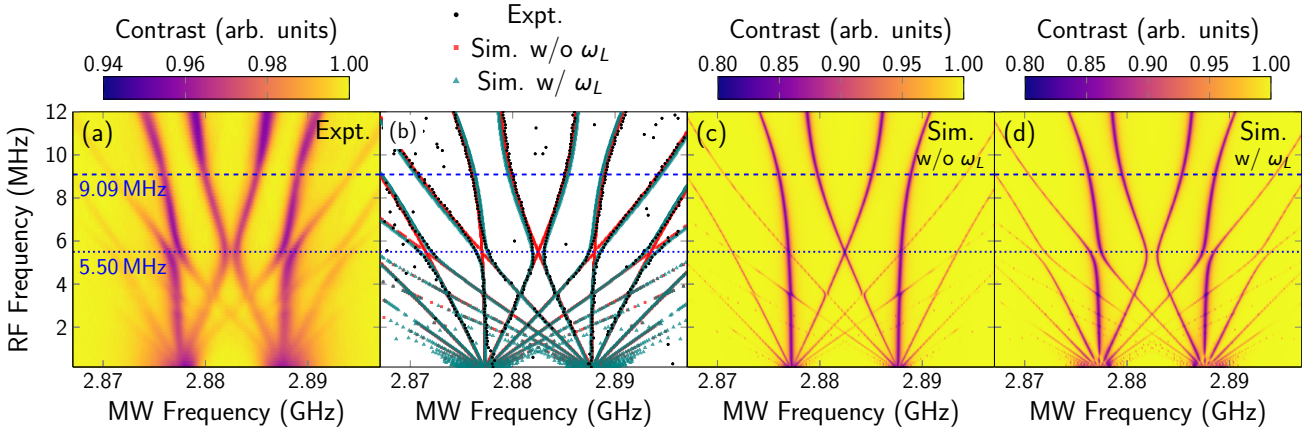

FIG. 3. (a) ESDR spectra under DC bias magnetic field perpendicular to NV axis as measured by sweeping MW frequencies and RF frequencies under strong RF field with $B_{\rm RF} = 136.8\,\mu$T. (b) Comparison of extracted resonant frequencies obtained experimentally and those obtained from numerical simulations (c) and (d) under strong RF field. Experimental resonant frequencies were extracted from (a), and numerically determined were extracted from (c) and (d). (c) and (d) Results of numerical simulations performed using Floquet Hamiltonian (c) without and (d) with parallel bias magnetic field. Parameters used are same as in Fig. 2. In (a)–(d), dashed lines indicate resonant frequency, $\omega_{\rm RF}/(2\pi) = 9.09\,$MHz, of single-RF-photon resonances, and dotted lines indicate resonant frequency, $\omega_{\rm RF}/(2\pi) = 5.50\,$MHz, of two-RF-photon resonances. There is good agreement between experimental results and those of theoretical calculations that consider parallel bias magnetic field. In contrast, theory without parallel bias magnetic field could not reproduce anticrossing structures induced by two-RF-photon resonances.

was approximately 5.5 MHz, as indicated by the dotted line in Fig. 3(a). The resonant RF frequency, $\omega_{\rm RF}/(2\pi)$, corresponding to these additional anticrossing structures were slightly different from the half of the energy gap between $|B'\rangle$ and $|D'\rangle$, that is, 4.54 MHz. This was owing to the Bloch-Siegert shift [56] because of the large anticrossing structures near the RF frequency $\omega_{\rm RF}/(2\pi) =$ 9.09 MHz. To quantify the Bloch-Siegert shift, we can use the analytical solutions, $\omega_{\rm MW} \approx \tilde{M}_x + \Omega_{\rm RF}^2/\tilde{M}_x$, derived from a simple model, and estimate the Bloch-Siegert shift as $\omega_{\rm RF}/(2\pi) \approx 5.24\,$MHz, as discussed in Appendix C.

Figures 3(c) and 3(d) show the results of the numerical simulations of the truncated Floquet Hamiltonians (dimensions of 405×405) in Eqs. (8) and (17), respectively. Both simulations in Figs. 3(c) and 3(d) could reproduce the anticrossing structures around the RF frequency $\omega_{\rm RF}/(2\pi) = 9.09\,$MHz as well as the sideband resonances. However, the anticrossing structures specific to the strong RF field would not be reproduced by the simulations without the parallel bias magnetic field, ω_L. In contrast, the simulation with the parallel bias magnetic field, ω_L, could reproduce the anticrossing structures around the RF frequency, $\omega_{\rm RF}/(2\pi) = 5.5\,$MHz. For comparison, we extracted the resonant frequencies from Figs. 3(a) and 3(c) and plotted them in Figs. 3(b) and 3(d), respectively. The numerical results obtained considering parallel bias magnetic field, ω_L, shown in Fig. 3(d) agreed with the experimental results shown in Fig. 3(a). Therefore, the anticrossing structures specific to the strong RF field are induced by the two-RF-photon resonances allowed by the parallel bias magnetic field, as discussed in Sec. II B.

In this study, we only demonstrated single-RF-photon and two-RF-photon resonances. However, in principle, it should be possible to observe the anticrossing structures owing to the more RF-photon resonances by using a stronger RF field.

E. Validity for analytical solutions

In the third experiment, we fixed the RF frequency, $\omega_{\rm RF}/(2\pi)$, to 9.09 MHz while changing the RF amplitude, $B_{\rm RF}$, and measured the ESDR, as shown in Fig. 4(a). As discussed in Refs. [16, 20], the anticrossing gaps induced by single-RF-photon resonances increase linearly with an increase in the RF amplitude, $B_{\rm RF}$. We adopted the analytical solutions described by Eqs. (11), (12), and (22) and attempted to fit the experimental results using them. In both cases, the calculation results agreed with the experimental ones. Moreover, the analytical solution in Eq.(22) reproduced even the resonant frequencies of the sidebands. However, because we used the RWA to derive the analytical solutions in Eqs. (11), (12), and (22), these solutions will not be valid for strong RF fields. When the Rabi frequency of the RF field is larger than half the resonant RF frequency ($\Omega_{\rm RF} > \omega_{\rm RF}/2$) [25, 36], the RWA is usually invalid. The analytical solutions in Eqs. (11), (12), and (22) started to deviate from the experimental results at frequencies higher than the Rabi frequency, $\Omega_{\rm RF} > 4.54\,$MHz (this RF amplitude is indicated by the dotted line in Figs. 4(a) and 4(b)).

To observe the two-RF-photon resonances, we measured the ESDR by setting the RF frequency as 4.54 MHz

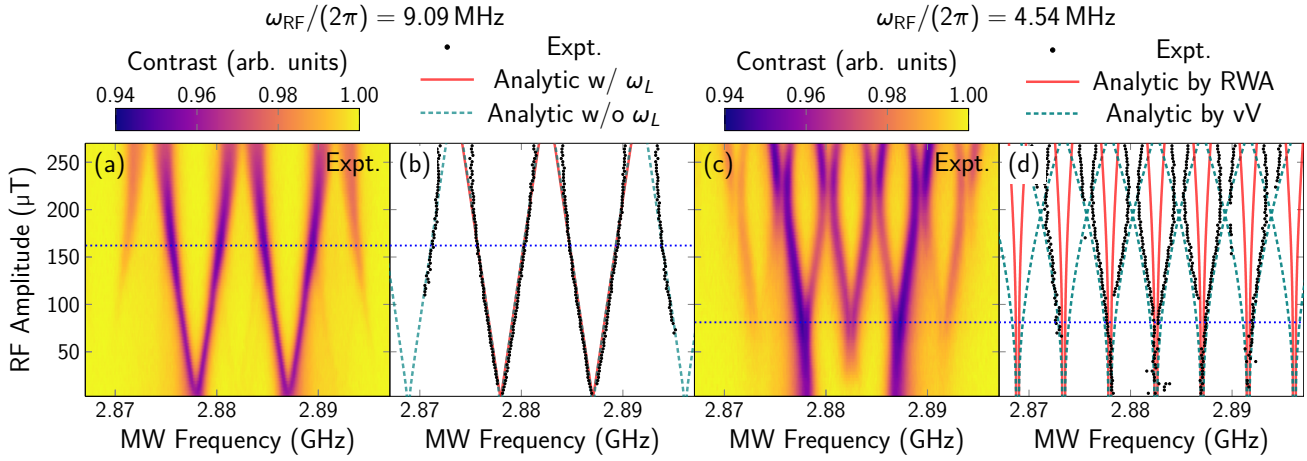

FIG. 4. (a) and (c) ESDR spectra under bias magnetic field perpendicular to NV axis as measured by changing RF amplitude B_{RF} while keeping the RF frequency at (a) $\omega_{RF}/(2\pi) = 9.09$ MHz (single-RF-photon resonance) and (c) 4.54 MHz (two-RF-photon resonance). (b) Comparison of resonant frequencies extracted from (a) and the analytical solutions given by Eqs. (11), (12), and (22). Analytical solutions obtained using Eqs. (11), (12), and (22) which were obtained with and without a parallel DC magnetic field, respectively, agree with experimental results. (d) Comparison of resonant frequencies extracted from (c) and those obtained from analytical solutions given by Eq. (22), which was based on RWA, and in Eq. (27), which was based on vV transformation. In (a) and (b) [(c) and (d)], dotted lines indicate boundaries of RWA conditions $\Omega_{RF} > \omega_{RF}/2$ [25, 36], which was calculated from $\omega_{RF}/(2\pi) = 9.09$ MHz, [4.54 MHz]. Analytical solutions given by Eqs. (11), (12), and (22) use RWA, which starts being violated in area above dotted line. In contrast, analytical solution given by Eq. (27) does not use RWA and can reproduce resonant frequencies beyond RWA conditions.

while changing the RF amplitude. The results are shown in Fig. 4(c). The resonant RF frequencies of the two-RF-photon resonances were smaller than those of the single-RF-photon resonances. This implies that the RWA is violated for smaller RF amplitudes. Thus, we used the vV transformation to obtain the analytical solutions that would be valid for a strong RF field. In Fig. 4(d), the experimentally measured resonant frequencies are plotted. In addition, we compared the results with the resonant frequencies calculated using the RWA and the vV transformation (See Eqs. (22) and (27)). When we used the analytical solutions with the RWA, we could not reproduce the experimental results for a strong RF field as shown in Fig. 4(d). This is because the RWA is violated for $\Omega_{RF} > 2.27$ MHz (indicated by the dotted line in Fig. 4(d)). However, the results obtained using the vV transformation (indicated by the dashed line) were in better agreement with the experimental results, as shown in Fig. 4(d). This is because we considered a higher-order correction, as mentioned in Sec.II C.

IV. CONCLUSIONS AND FUTURE PROSPECTS

In this study, we theoretically and experimentally investigated the phenomenon of ESDR under strong RF fields. We observed the anticrossing structures attributable to multi-RF-photon resonances and reproduced the ESDR spectra of the NV centers through numerical simulations based on the Floquet theory. Moreover, using the vV transformation, we derived analytical solutions for the anticrossing structures observed under the strong RF field. Our results provide new insights into the phenomenon of ESDR, including the mechanism responsible for the anticrossing structures and the role of a parallel magnetic field. In addition, they should aid in the realization of practical RF sensors with NV centers and allow for the exploration of Floquet engineering in open quantum systems.

Lastly, we discuss the direction for future work on the topic. Firstly, these results will aid the realization of practical RF sensors based on the CW-ODMR of NV centers. Our previous understanding of the effect of a strong RF field on the phenomenon of ESDR was limited. Because we elucidated the mechanism of the ESDR under strong RF fields, it should be possible to develop practical RF sensors with a wider dynamic range.

Next, the results of this study should help simulate various quantum phenomena in strong driving fields. Floquet engineering, which involves the creation of quantum systems with desired properties using a driving field has succeeded in realizing various quantum phenomena [30]. In such experiments, the quantum systems are well-designed isolated systems; the dissipation can be negligible [40–42]. However, most materials interact with the environment in reality, and their dissipation is not negligible. Moreover, it is usually difficult to detect the quantum states of such materials [57]. Therefore, it is necessary to extend Floquet engineering to open quantum systems. Because the NV center is robust to dissipation by the environment, and its spin state can be easily

manipulated and readout with high fidelity, it is an ideal model for Floquet engineering in open systems [40, 41]. Strong driving (or multi-photon) phenomena in NV centers have been reported using different methods and setups [23, 24, 37, 46, 47, 58]. However, in most previous studies, an MW field was used instead of an RF field. Because it is easier to go beyond the RWA regime in the case of RF fields compared with the MW, our approach may be more promising for observing phenomena owing to the breakdown of the approximation. Although a few studies have used an RF field, one needs to use multiple driving fields to realize strong driving phenomena; this results in high power consumption and requires complex control. Therefore, generating RF-dressed states using their approaches is not straightforward.

ACKNOWLEDGMENTS

We thank Dr. Kento Sasaki, Prof. Kensuke Kobayashi, and Dr. Ikeda N. Tatsuhiko for their valuable discussions. This work is supported by MEXT KAKENHI(20H05661, 22H01558), MEXT Q-LEAP(No. JPMXS0118067395), Leading Initiative for Excellent Young Researchers MEXT Japan, JST presto (Grant No. JPMJPR1919) Japan, JST (Moonshot R&D)(Grant Number JPMJMS226C), and Kanazawa University CHOZEN Project 2022.

APPENDIX A: EFFECT OF A PERPENDICULAR DC BIAS MAGNETIC FIELD

The Hamiltonian of the NV center under the bias magnetic field perpendicular to the NV axis is described as:

$$\hat{H}_0 = D_{\mathrm{GS}}\hat{S}_z^2 + M_x(\hat{S}_x^2 - \hat{S}_y^2) + \gamma_e B_x \hat{S}_x + \gamma_e B_y \hat{S}_y. \quad \text{(A1)}$$

Here, the strain is considered to be along the x-direction. It is difficult to diagonalize the Hamiltonian in Eq. (A1). Thus, we treat the bias magnetic field terms as a perturbation under the assumption that, $B_x, B_y \ll D_{\mathrm{GS}}$. From the second-order perturbation theory, the Hamiltonian in Eq. (A1) is rewritten as: [17, 18, 43]

$$\hat{H}_0 \approx \tilde{D}_{\mathrm{GS}}\hat{S}_z^2 + \tilde{M}_x(\hat{S}_x^2 - \hat{S}_y^2), \quad \text{(A2)}$$

where

$$\begin{aligned} \tilde{D}_{\mathrm{GS}} &:= D_{\mathrm{GS}} + \frac{3}{2}\left(\frac{\|\gamma_e B_x\|^2}{D_{\mathrm{GS}} + M_x} + \frac{\|\gamma_e B_y\|^2}{D_{\mathrm{GS}} - M_x}\right), \\ \tilde{M}_x &:= M_x + \frac{1}{2}\left(\frac{\|\gamma_e B_x\|^2}{D_{\mathrm{GS}} + M_x} - \frac{\|\gamma_e B_y\|^2}{D_{\mathrm{GS}} - M_x}\right). \end{aligned} \quad \text{(A3)}$$

APPENDIX B: FLOQUET THEORY

Let us consider the time-dependent Schrödinger equation with a time-periodic Hamiltonian ($\hbar = 1$):

$$\hat{H}(t)\,|\psi(t)\rangle = i\frac{\mathrm{d}}{\mathrm{d}t}\,|\psi(t)\rangle, \quad \hat{H}(t) = \hat{H}(t+T), \quad \text{(B1)}$$

where $T = 2\pi/\omega$ denotes the time periodicity. Using Floquet's theorem, which is similar to Bloch's theorem, the solution of Eq. (B1) can be written as a linear combination of the Floquet states, as follows:

$$|\psi_\alpha(t)\rangle = e^{-i\varepsilon_\alpha t}\,|\phi_\alpha(t)\rangle\,, \quad \text{(B2)}$$

Here, $|\phi_\alpha(t)\rangle = |\phi_\alpha(t+T)\rangle$ is the Floquet mode and ε_α is called the quasi-energy. We use the Fourier expansion,

$$\hat{H}(t) = \sum_m \hat{H}^{(m)} e^{im\omega t}, \;\; |\phi_\alpha(t)\rangle = \sum_m e^{im\omega t}\,|\phi_\alpha^{(m)}\rangle\,, \quad \text{(B3)}$$

where $\hat{H}^{(n)}$ and $|\phi_\alpha^{(n)}\rangle$ are the n-th Fourier coefficients of $\hat{H}(t)$ and $|\phi_\alpha^{(m)}\rangle$, respectively. On substituting these into Eq. (B1), we obtain the infinite-dimensional time-independent eigenvalue equation [27]

$$\sum_m \left[\hat{H}^{(n-m)} + m\omega\delta_{m,n}\hat{1}\right]|\phi_\alpha^{(m)}\rangle = \varepsilon_\alpha\,|\phi_\alpha^{(n)}\rangle\,, \quad \text{(B4)}$$

where $\delta_{m,n}$ is the Kronecker delta and $\hat{1}$ is the identity operator. For convenience, we introduce the extended Hilbert space or the Sambe space, $\mathfrak{F} := \mathfrak{H} \otimes \mathfrak{T}$ [28], where $\mathfrak{H}$ and $\mathfrak{T}$ are the Hilbert spaces for the quantum states and T-periodic functions, respectively. A quantum state $e^{in\omega t}\,|\alpha\rangle$ in the Hilbert space corresponds to $|\alpha, n\rangle := |\alpha\rangle \otimes |n\rangle$ in the Hilbert space. Moreover, we use the Floquet ladder operators $\hat{F}_n$ and the Floquet number operator, $\hat{N}$, as defined in [31]:

$$\hat{\mathcal{F}}_n\,|m\rangle = |n+m\rangle\,, \quad \hat{\mathcal{N}}\,|n\rangle = n\,|n\rangle\,. \quad \text{(B5)}$$

Then, Eq. (B4) can be simply written as

$$\hat{H}_F\,|\phi_\alpha\rangle = \varepsilon_\alpha\,|\phi_\alpha\rangle\,, \quad \text{(B6)}$$

where $\hat{H}_F$ is the Floquet Hamiltonian defined as

$$\hat{H}_F := \sum_m \hat{\mathcal{F}}_m \otimes \hat{H}^m + \hat{\mathcal{N}} \otimes \omega\hat{1} \quad \text{(B7)}$$

$$= \begin{bmatrix} \ddots & \vdots & \vdots & \vdots & \\ \cdots & \hat{H}^{(0)} + \omega\hat{1} & \hat{H}^{(+1)} & \hat{H}^{(+2)} & \cdots \\ \cdots & \hat{H}^{(-1)} & \hat{H}^{(0)} & \hat{H}^{(+1)} & \cdots \\ \cdots & \hat{H}^{(-2)} & \hat{H}^{(-1)} & \hat{H}^{0} - \omega\hat{1} & \cdots \\ & \vdots & \vdots & \vdots & \ddots \end{bmatrix}. \quad \text{(B8)}$$

Therefore, the Floquet theory can be used to convert the time-dependent Schrödinger equation given in Eq. (B1) into an eigenvalue problem of the infinite-dimensional, time-independent Hamiltonian given in Eq. (B8).

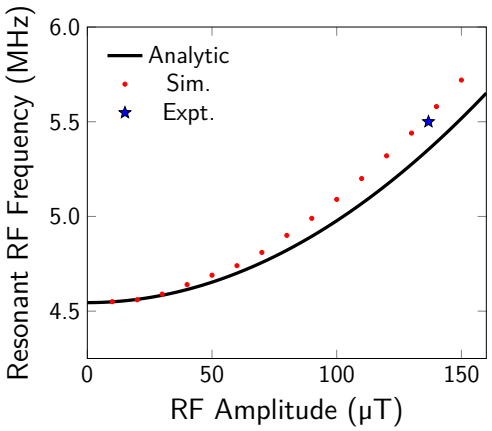

FIG. 5. Comparison of the resonant RF frequencies for two-RF-photon resonances between the analytical solutions given by $\omega_{\rm RF} \approx \tilde{M}_x + \Omega_{\rm RF}^2/\tilde{M}_x$, the numerical results, and the experimental results extracted in Fig. 3(a).

APPENDIX C: EVALUATION OF THE BLOCH-SIEGERT SHIFT

In this section, we discuss ways to qualify the Bloch-Siegert shift. Here, we focus on the two-RF-photon resonance between $|B,-1\rangle$ and $|D,+1\rangle$, which occurred around the MW frequency, $\omega_{\rm MW} \approx 2.8825\,$GHz. The two-RF-photon resonance occurs where the resonant MW frequency of $|B,-1\rangle$ is the same as that of $|D,+1\rangle$ with respect to the single-RF-photon resonances. Finding such a condition from Eqs. (11) and (12), we obtain

$$\omega_{\rm RF} \approx \tilde{M}_x + \Omega_{\rm RF}^2/V. \tag{C1}$$

Thus, under the strong RF field with $B_{\rm RF} \approx 136.8\,\mu$T, the Bloch-Siegert shift is calculated as $\omega_{\rm RF}/(2\pi) \approx 5.24\,$MHz. There is a small difference between the experimental value of 5.50 MHz and the analytical value of 5.24 MHz. This is because we adopted a perturbative approach to derive the analytical value, which is valid only when the RF amplitude is weak. On the other hand, as shown in Fig. 5, the numerical simulation without the perturbation effectively reproduced the experimental results. Moreover, as the RF amplitude was reduced, the value from the analytical solution became closer to that from the numerical simulation. This behavior is consistent with the fact that we used the perturbation theory.

[1] E. V. Levine, M. J. Turner, P. Kehayias, C. A. Hart, N. Langellier, R. Trubko, D. R. Glenn, R. R. Fu, and R. L. Walsworth, Nanophotonics **8**, 1945 (2019).
[2] J. F. Barry, J. M. Schloss, E. Bauch, M. J. Turner, C. A. Hart, L. M. Pham, and R. L. Walsworth, Rev. Mod. Phys. **92**, 015004 (2020).
[3] M. J. Ku, T. X. Zhou, Q. Li, Y. J. Shin, J. K. Shi, C. Burch, L. E. Anderson, A. T. Pierce, Y. Xie, A. Hamo, U. Vool, H. Zhang, F. Casola, T. Taniguchi, K. Watanabe, M. M. Fogler, P. Kim, A. Yacoby, and R. L. Walsworth, Nature **583**, 537 (2020).
[4] W. S. Huxter, M. L. Palm, M. L. Davis, P. Welter, C.-H. Lambert, M. Trassin, and C. L. Degen, Nat. Commun. **13**, 3761 (2022).
[5] W. S. Huxter, M. F. Sarott, M. Trassin, and C. L. Degen, Nat. Phys. (2023), 10.1038/s41567-022-01921-4.
[6] E. Boyers, P. J. D. Crowley, A. Chandran, and A. O. Sushkov, Phys. Rev. Lett. **125**, 160505 (2020).
[7] W. Zhang, X. Ouyang, X. Huang, X. Wang, H. Zhang, Y. Yu, X. Chang, Y. Liu, D.-L. Deng, and L.-M. Duan, Phys. Rev. Lett. **127**, 90501 (2021).
[8] K. Yang, S. Xu, L. Zhou, Z. Zhao, T. Xie, Z. Ding, W. Ma, J. Gong, F. Shi, and J. Du, Phys. Rev. B **106**, 184106 (2022).
[9] J. M. Schloss, J. F. Barry, M. J. Turner, and R. L. Walsworth, Phys. Rev. Appl. **10**, 34044 (2018).
[10] M. Tsukamoto, K. Ogawa, H. Ozawa, T. Iwasaki, M. Hatano, K. Sasaki, and K. Kobayashi, Appl. Phys. Lett. **118**, 264002 (2021).
[11] B. Chen, B. Chen, X. Zhu, J. Fan, Z. Yu, P. Qian, and N. Xu, Rev. Sci. Instrum. **93**, 125105 (2022).
[12] S. Simon, G. Tuvia, F. M. Stürner, U. Thomas, W. Gerhard, M. Christoph, S. Jochen, N. Boris, M. Matthew, P. Sebastien, M. Jan, S. Ilai, P. Martin, R. Alex, L. P. McGuinness, and J. Fedor, Science **356**, 832 (2017).
[13] J. M. Boss, K. S. Cujia, J. Zopes, and C. L. Degen, Science **356**, 837 (2017).
[14] C. A. Hart, J. M. Schloss, M. J. Turner, P. J. Scheidegger, E. Bauch, and R. L. Walsworth, Phys. Rev. Appl. **15**, 44020 (2021).
[15] G. Wang, Y.-X. Liu, J. M. Schloss, S. T. Alsid, D. A. Braje, and P. Cappellaro, Phys. Rev. X **12**, 21061 (2022).
[16] S. Saijo, Y. Matsuzaki, S. Saito, T. Yamaguchi, I. Hanano, H. Watanabe, N. Mizuochi, and J. Ishi-Hayase, Appl. Phys. Lett. **113**, 082405 (2018).
[17] T. Yamaguchi, Y. Matsuzaki, S. Saito, S. Saijo, H. Watanabe, N. Mizuochi, and J. Ishi-Hayase, Jpn. J. Appl. Phys. **58**, 100901 (2019).
[18] H. Tabuchi, Y. Matsuzaki, N. Furuya, Y. Nakano, H. Watanabe, N. Tokuda, N. Mizuochi, and J. Ishi-Hayase, J. Appl. Phys. **133**, 24401 (2023).
[19] A. K. Dmitriev and A. K. Vershovskii, J. Phys. Conf. Ser. **1135**, 12051 (2018).
[20] A. K. Dmitriev, H. Y. Chen, G. D. Fuchs, and A. K. Vershovskii, Phys. Rev. A **100**, 11801 (2019).
[21] A. K. Dmitriev and A. K. Vershovskii, IEEE Sens. Lett. **4**, 1 (2020).
[22] A. K. Dmitriev and A. K. Vershovskii, Phys. Rev. A **105**, 43509 (2022).
[23] G. D. Fuchs, V. V. Dobrovitski, D. M. Toyli, F. J. Heremans, and D. D. Awschalom, Science **326**, 1520 (2009).

[24] P. London, P. Balasubramanian, B. Naydenov, L. P. McGuinness, and F. Jelezko, Phys. Rev. A **90**, 12302 (2014).

[25] J. Scheuer, X. Kong, R. S. Said, J. Chen, A. Kurz, L. Marseglia, J. Du, P. R. Hemmer, S. Montangero, T. Calarco, B. Naydenov, and F. Jelezko, New J. Phys. **16**, 093022 (2014).

[26] A. Laucht, S. Simmons, R. Kalra, G. Tosi, J. P. Dehollain, J. T. Muhonen, S. Freer, F. E. Hudson, K. M. Itoh, D. N. Jamieson, J. C. McCallum, A. S. Dzurak, and A. Morello, Phys. Rev. B **94**, 161302 (2016).

[27] J. H. Shirley, Phys. Rev. **138**, B979 (1965).

[28] H. Sambe, Phys. Rev. A **7**, 2203 (1973).

[29] A. Eckardt and E. Anisimovas, New J. Phys. **17**, 093039 (2015).

[30] T. Oka and S. Kitamura, Annu. Rev. Condens. Matter Phys. **10**, 387 (2019).

[31] K. L. Ivanov, K. R. Mote, M. Ernst, A. Equbal, and P. K. M, Prog. Nucl. Magn. Reson. Spectrosc. **126–127**, 17 (2021).

[32] S. K. Son, S. Han, and S. I. Chu, Phys. Rev. A **79**, 1 (2009).

[33] J. Hausinger and M. Grifoni, Phys. Rev. A **81**, 22117 (2010).

[34] C. Deng, J.-L. Orgiazzi, F. Shen, S. Ashhab, and A. Lupascu, Phys. Rev. Let. **115**, 133601 (2015).

[35] Y. Han, X.-Q. Luo, T.-F. Li, W. Zhang, S.-P. Wang, J. S. Tsai, F. Nori, and J. Q. You, Phys. Rev. Appl. **11**, 14053 (2019).

[36] G. Wang, Y.-X. Liu, and P. Cappellaro, Phys. Rev. A **103**, 22415 (2021).

[37] S. Nishimura, K. M. Itoh, J. Ishi-Hayase, K. Sasaki, and K. Kobayashi, Phys. Rev. Appl. **18**, 64023 (2022).

[38] I. Martin, G. Refael, and B. Halperin, Phys. Rev. X **7**, 41008 (2017).

[39] Q. Chen, H. Liu, M. Yu, S. Zhang, and J. Cai, Phys. Rev. A **102**, 52606 (2020).

[40] T. N. Ikeda and M. Sato, Sci. Adv. **6**, 1 (2020).

[41] T. Ikeda, K. Chinzei, and M. Sato, SciPost Phys. Core **4**, 033 (2021).

[42] T. Mori, Annu. Rev. Condens. Matter Phys. **14**, null (2023).

[43] C. S. Shin, C. E. Avalos, M. C. Butler, H.-J. Wang, S. J. Seltzer, R.-B. Liu, A. Pines, and V. S. Bajaj, Phys. Rev. B **88**, 161412 (2013).

[44] Y. Matsuzaki, H. Morishita, T. Shimooka, T. Tashima, K. Kakuyanagi, K. Semba, W. J. Munro, H. Yamaguchi, N. Mizuochi, and S. Saito, J. Condens. Matter Phys. **28**, 275302 (2016).

[45] H. Morishita, T. Tashima, D. Mima, H. Kato, T. Makino, S. Yamasaki, M. Fujiwara, and N. Mizuochi, Sci. Rep. **9**, 13318 (2019).

[46] L. Childress and J. McIntyre, Phys. Rev. A **82**, 33839 (2010).

[47] J. Meinel, V. Vorobyov, B. Yavkin, D. Dasari, H. Sumiya, S. Onoda, J. Isoya, and J. Wrachtrup, Nat. Commun. **12**, 2737 (2021).

[48] Y. Han, X. Q. Luo, T. F. Li, and W. Zhang, Phys. Rev. A **101**, 022108 (2020).

[49] M. Leskes, P. K. Madhu, and S. Vega, Prog. Nucl. Magn. Reson. Spectrosc. **57**, 345 (2010).

[50] G. Wang, Y.-X. Liu, Y. Zhu, and P. Cappellaro, Nano Lett. **21**, 5143 (2021).

[51] J. Michl, T. Teraji, S. Zaiser, I. Jakobi, G. Waldherr, F. Dolde, P. Neumann, M. W. Doherty, N. B. Manson, J. Isoya, and J. Wrachtrup, Appl. Phys. Lett. **104**, 102407 (2014).

[52] M. Lesik, J.-P. Tetienne, A. Tallaire, J. Achard, V. Mille, A. Gicquel, J.-F. Roch, and V. Jacques, Appl. Phys. Lett. **104**, 113107 (2014).

[53] T. Fukui, Y. Doi, T. Miyazaki, Y. Miyamoto, H. Kato, T. Matsumoto, T. Makino, S. Yamasaki, R. Morimoto, N. Tokuda, M. Hatano, Y. Sakagawa, H. Morishita, T. Tashima, S. Miwa, Y. Suzuki, and N. Mizuochi, Appl. Phys. Express **7**, 55201 (2014).

[54] H. Ishiwata, M. Nakajima, K. Tahara, H. Ozawa, T. Iwasaki, and M. Hatano, Appl. Phys. Lett. **111**, 43103 (2017).

[55] K. Sasaki, Y. Monnai, S. Saijo, R. Fujita, H. Watanabe, J. Ishi-Hayase, K. M. Itoh, and E. Abe, Rev. Sci. Instrum. **87**, 053904 (2016).

[56] F. Bloch and A. Siegert, Phys. Rev. **57**, 522 (1940).

[57] K. Uchida, S. Kusaba, K. Nagai, T. N. Ikeda, and K. Tanaka, Science Advances **8**, eabq728 (2022).

[58] T. Tashima, H. Morishita, and N. Mizuochi, Phys. Rev. A **100**, 23801 (2019).